




Nanocellulose intercalation to boost the performance of MXene pressure sensor for human interactive monitoring

Jie Yang¹, Hui Li¹, Jianli Cheng^{1,*}, Tao He¹, Jinshan Li¹, and Bin Wang^{1,*} 

¹Institute of Chemical Materials, China Academy of Engineering Physics, Mianyang 621900, Sichuan, China

Received: 1 November 2020

Accepted: 8 February 2021

Published online:

25 May 2021

© The Author(s), under exclusive licence to Springer Science+Business Media, LLC, part of Springer Nature 2021

ABSTRACT

The advent of smart and wearable electronics endows flexible pressure sensors with promising potentiality. $Ti_3C_2T_x$ -based MXene is considered as one of attractive sensing materials for its metallic conductivity and adjustable interlayer. However, existing flexible MXene pressure sensor still requires a technical breakthrough that simultaneously possessing high sensitivity, fast response, and durability in low-pressure regime and excellent mechanical strength. Herein, a $Ti_3C_2T_x$ -based pressure sensor with distinctly enhanced sensing functionality and mechanical strength is demonstrated through inserting high-strength of bacterial cellulose nanofibers to control the interlayer of MXene. By optimizing the bacterial cellulose content and MXene interlayer space, the resultant sensor device exhibits high mechanical strength (225 MPa), wide-sensing range with low detective limit (0.4 Pa), high sensitivity (up to 95.2 kPa^{-1} , in $< 50 \text{ Pa}$ region), fast response (95 ms) and outperformed repeatability (25,000 cycles), as well as low operation voltage of 0.1 V. For practical application demos, the sensor can monitor multiple human biologic activities, including subtle pressures (e.g., swallow, heartbeat and pulse), acoustic vibrations and gesture motions, and serve as electronic skin for mapping pressure distribution, elucidating the potential application in medical diagnosis, smart robotics and human-machine interfacing.

Introduction

With the rapid advances of portable and wearable electronics, the flexible pressure sensor, which can be applied in health-care monitors, medical diagnosis

and future electronic skins, has attracted considerable interests in recent years [1, 2]. Among different working mechanisms based pressure sensors including piezoresistive [3, 4], capacitive [5, 6] and triboelectric effects [1], the piezoresistive pressure

Handling Editor: Stephen Eichhorn.

Address correspondence to E-mail: jianlicheng@caep.cn; binwang@caep.cn

<https://doi.org/10.1007/s10853-021-05909-y>

sensor is one of the most popularly used one because of its high sensitivity, fast frequency response and outstanding durability and repeatability, as well as facile fabrication [7]. While a pressure is loaded, the contact area of sensing material is changed, leading to the variation of the electrical property and thereby generating the current/resistance signal. Since the last few years, many endeavors have been devoted and various novel materials with nano/microstructures have been extensively employed to achieve excellent sensing performance [8–10]. Graphene nanosheets [3, 11–13], carbon nanotubes (CNTs) [14], metal nanowires [15], conductive polymers [16] and some emerging materials such as biomass carbon [17], conductive foam/aerogels have been broadly explored as potential materials to improve their piezoresistive performances [4, 18]. For instance, Ren et al realized a pressure sensor with a sensitivity of 17.2 kPa^{-1} and a detection limit of 10.0 Pa based on a graphene paper [12]. Xu et al prepared a carbonized crepe paper-based pressure sensor and achieved a sensitivity of 5.67 kPa^{-1} and a detection limit of 0.9 Pa [19]. In another work, Peng et al reported an aerogel pressure sensor with conductive carbon black as the sensing material through three-dimensional (3D) print method with a sensitivity of up to 5.54 kPa^{-1} in the range of $10 \sim 800 \text{ kPa}$ [4]. Although great progress has already achieved for developing highly sensitive pressure sensor, comprehensive performances including low working potential, high sensitivity, long stability, wide-sensing range and fast response time are still far beyond practical requirements. The challenge on constructing flexible pressure sensor mainly remains in how to design and synthesize flexible sensor materials with comprehensive sensing activity. Furthermore, the characteristics of inner atomic structure of conventional piezoresistive materials make them difficult to further enhance the sensing performance due to the ultrahigh resistance of atomic movement [20]. In this regard, exploring the new materials and structures with superior comprehensive sensing performances underlies the foundation for high-performance pressure sensors of wearable electronics.

As an emerging family of two-dimensional (2D) transition metal carbides and nitrides, MXenes receive enormous interest in electrochemical application such as supercapacitors [21–23], batteries [24, 25] and catalyst [26] due to metallic electrical conductivity and hydrophilic pseudocapacitive

surface [27, 28]. More importantly, the MXenes own a lamellar structure with abundant hydrophilic groups on the surface and thereby exhibiting relatively adjustable conductivity by the changeable interlayers distance under certain pressure, enabling MXene to serve as promising candidate materials for highly sensitive pressure sensor [20, 29–32]. Recently, Gao et al developed a pressure sensor used pure multi-layer $\text{Ti}_3\text{C}_2\text{T}_x$ -based MXene as sensing materials, achieving a gauge factor (GF) of 180 and a detection limit of 10.5 Pa [20]. Yu et al presented a flexible and degradable pressure sensor by attaching MXene-impregnated tissue paper on a biodegradable polylactic acid substrate, exhibiting a sensitivity of 3.81 kPa^{-1} and a low-detection limit of 10.2 Pa as well as great reproducibility over 10,000 cycles and excellent degradability [7]. To further improve the sensitivity, another promising strategy is employed MXene-based foam/aerogel with high porosity and deformability as functional sensing materials [33–36]. For example, Ma et al presented a $\text{Ti}_3\text{C}_2\text{T}_x$ /reduced graphene oxide (RGO) foam pressure sensor, which delivers the sensing performance with sensitivity (22.56 kPa^{-1}), response time (245 ms), detection limit of 10.0 Pa and mechanical stability of 10,000 cycles [33]. Sun et al demonstrated a carbonized $\text{Ti}_3\text{C}_2\text{T}_x$ /BC aerogel with a wave-shaped lamella structure to decrease detection limit, and the sensing performance with sensitivity (12.5 kPa^{-1}), response time (167 ms), detection limit of 1.0 Pa and operating potential (1.0 V) and repeatability of 1000 cycles was obtained [36]. Nevertheless, several shortcomings for the flexible MXene-based pressure sensor are still needed to be addressed. Firstly, ultrahigh intrinsic conductivity and limited compression rate of interlayer space of MXene cause very high initial current value which results in a small conducting pathway change in the subtle pressure loadings, thus limiting the sensitivity for piezoresistive sensors [37]. At the same time, MXene foam/aerogel materials with high compression rate can significantly enhance the sensitivity, detection limit and responsive time, but the poor mechanical strength makes them hard to meet the long-term deformation requirements, especially for large pressure response. In addition, most MXene-based pressure sensors were fabricated by combining sensing materials with polymer substrate/supporter such as polydimethylsiloxane (PDMS), tissue to improve the mechanical strength. Unfortunately, the sensitivity, response time and durability were

lessened to some extent due to the reduced deformation and poor bond ability [38, 39]. Moreover, the detective limit is not very low because of the flexural response pathway and interference of the substrate. As known, detection limit and sensitivity are very crucial to determine the application field of pressure sensor, especially for the use in the highly sensitive human biological activities and electronic skin. Thus, designing MXene pressure sensor with innovative nano/microstructure of that combine high compression rate of interlayer space and enough mechanical strength is a wise strategy to meet the above requirements.

Bacterial cellulose (BC) as a widely used nanocellulose consists of ultrafine interconnected nanofibers with plenty of oxygen-containing functional groups in the polymer chains, which can serve as an excellent pressure-accommodating buffer due to high tensile strength and good hydrophilicity originated from the spontaneous hydrogen bond interaction [40–42]. Although the strain sensor based on carbon aerogel prepared by annealing BC/MXene composite has been reported recently [43], the sensing performances especially for low-detection limits and response/recovery time are far beyond satisfactory due to the limited change of layer space between the carbonized carbon originated from BC and MXene. Different from the reported MXene hybrid aerogels using BC as the nanobinder, in this work, we report a self-assembled intercalation hybrid film by integrating few-layered $\text{Ti}_3\text{C}_2\text{T}_x$ nanosheets with BC nanofibers to significantly enhance the sensing performance of

pressure sensor under mechanical stimulus (Fig. 1a). On one hand, the importing of BC nanocellulose, not only provides a highly flexible buffer to enhance the layer separation of MXenes but also ensures the good material integrity by hydrogen bond interactions to achieve high mechanical strength of the hybrid film. On the other hands, the intercalation of nanocelluloses into the interlayer of single few-layered MXene can bring in more interlayer space and efficient MXene utilization, which can improve the conductive pathways and significantly promote sensing activity for both sensitivity, limit of detection and wide-sensing range. Based on the aforementioned advantages, the fabricated pressure sensor demonstrates superior sensing performances with high sensitivity (up to 95.2 kPa^{-1} , $<50 \text{ Pa}$), fast response (95 ms), wide-sensing range with a low limit of detection of 0.4 Pa and low operating potential (0.1 V) as well as excellent mechanical stability (25,000 cycles). As a proof of concept, we demonstrate that the pressure sensor can not only attach to different positions of human body for wide-sensing range health-care monitoring including tiny pressures (e. g. pulse, heartbeat), acoustic vibrations and large bending movements (e. g. arm bending, knee motion), but also serve as interactive spatial pressure distribution sensor, indicating the promising potential for medical diagnosis, electronic skin and human-machine interfacing.

Materials and methods

Materials availability

The Ti_3AlC_2 MAX was acquired from Jilin 11 Tech. Co., Ltd., and hydrochloric acid (HCl, 36%) and lithium fluoride (LiF, 99.7%) were brought from Chengdu Kelong reagent factory. The bacterial cellulose suspension (BC, 0.5%) was acquired from Macklin reagent company. All the above reagents were directly used without further purification. The deionized (DI) water was produced with ultrapure water equipment (ULUP-I, Sichuan ULUPURE Ltd., Co.).

Preparation of few-layered $\text{Ti}_3\text{C}_2\text{T}_x$ nanosheets

Few-layered $\text{Ti}_3\text{C}_2\text{T}_x$ nanosheets were prepared by traditional selectively etching and ultra-sonication

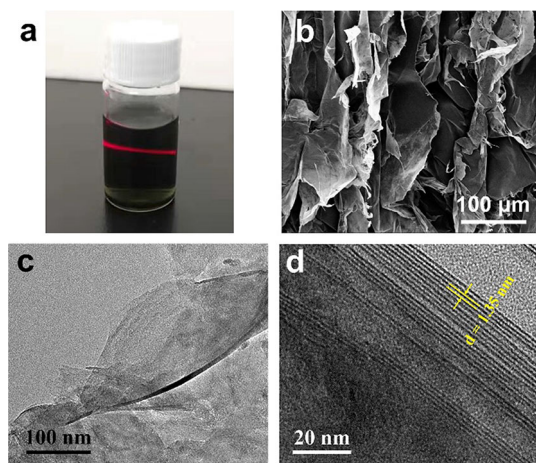


Figure 1 a Photograph of few-layered $\text{Ti}_3\text{C}_2\text{T}_x$ nanosheets suspension with a significant Tyndall effect; b SEM and c-d TEM images of the few-layered $\text{Ti}_3\text{C}_2\text{T}_x$ nanosheets.

exfoliation of Ti_3AlC_2 MAX phase. Typically, 1.0 g LiF powder and 20 mL HCl (9.0 mol L^{-1}) solution were mixed and stirred for 10 min, and then, 1.0 g Ti_3AlC_2 powder was added. After reacting at 35°C for 24 h, the resultant product was washed with DI water and centrifuged at 8,000 rpm for several times until the supernatant pH of > 6 . Afterward, clay-like $\text{Ti}_3\text{C}_2\text{T}_x$ was dispersed in ethanol and ultra-sonicated for 2.0 hours to obtain exfoliated $\text{Ti}_3\text{C}_2\text{T}_x$ nanosheets. The exfoliated $\text{Ti}_3\text{C}_2\text{T}_x$ nanosheets dispersion was centrifuged at 10,000 rpm to remove ethanol and re-dispersed in 60 mL DI water. After ultra-sonication and centrifugation at 3,500 rpm for 10 min, a stable colloid suspension of few-layered $\text{Ti}_3\text{C}_2\text{T}_x$ nanosheets was obtained.

Preparation of $\text{Ti}_3\text{C}_2\text{T}_x/\text{BC}$ composite (TB) film

0.1 wt.% bacterial cellulose (BC) suspension mixed with different mass ratios of $\text{Ti}_3\text{C}_2\text{T}_x$ dispersion (0.5 mg mL^{-1}) and ultra-sonicated for 5 min for homogenization. To prepare $\text{Ti}_3\text{C}_2\text{T}_x/\text{BC}$ composite film, above $\text{Ti}_3\text{C}_2\text{T}_x/\text{BC}$ mixture with same solid content was vacuum filtered with a membrane filter ($0.45 \mu\text{m}$ pore size). Once no flowable liquid was left on the film surface, the vacuum was released immediately. The filter membrane along with $\text{Ti}_3\text{C}_2\text{T}_x/\text{BC}$ film was transferred into -30°C circumstance to freeze for 24 h, then freeze-dried for 24 h to obtain the TB composite film. The TB films with solid mass ratio of $\text{Ti}_3\text{C}_2\text{T}_x/\text{BC}$ of 0.25, 0.5, 1.0, 1.5, 2.0 and 4.0 were named as TB-0.25, TB-0.5, TB-1, TB-1.5, TB-2 and TB-4, respectively.

Materials characterization

The diffraction patterns were characterized by X-ray diffraction (XRD, D/Max-2004) with $\text{Cu K}\alpha$ radiation ($\lambda=1.5418\text{\AA}$). The scanning electron microscope (SEM) images were acquired with a field emission scanning electron microscope combine with an energy-dispersive spectrometer (EDS) (Hitachi SU8010, Japan). The transmittance electron microscopy (TEM) images were obtained with a JEM-2100F transmittance electron microscopy operated at 200 kV and the optical images were taken by a digital camera (Nikon, J1). To estimate the mechanical strength, the stress–strain curves of different films with an effective size of 20×5 (length \times width) mm^2 were

measured by employing electronic tensile strength tester (LLY-06E). The gauge length and strain rate were set as 10 mm and 10 mm min^{-1} , respectively. The mechanical strength values of different films were obtained by averaging the results of three parallel test.

Pressure sensor assembly and test

To evaluate the sensing properties of $\text{Ti}_3\text{C}_2\text{T}_x/\text{BC}$ composite film, a piece of TB film ($5\times 10 \text{ mm}^2$) was fixed on a $10\times 10 \text{ mm}^2$ -sized flexible Au interdigital electrode with polyimide tape and connected with copper conductive wire. A home-made testing system includes a programmable step-motor, and a commercial force sensor was used for the sensing performance test. The I - V and real-time I - t curves were recorded with an VSP-300 (Bio-Logic SAS, France) electrochemical workstation. An input voltage bias of 0.1 V was selected during the sensing test process. The sensitivity of different pressure sensors was calculated with equation of $S = [(I - I_0)/I_0]/P$, where the I_0 and I , respectively, represent real-time current without and with a certain pressure loading, P is the value of pressure loading [4].

Results and discussion

Materials characterization

The suspension of $\text{Ti}_3\text{C}_2\text{T}_x$ nanosheets was prepared through an in situ selectively etching and an ultra-sonic exfoliation process. As shown in Fig. 1a, the suspension of $\text{Ti}_3\text{C}_2\text{T}_x$ nanosheets exhibits a stably colloidal dispersion with typical Tyndall scattering effect. SEM and TEM images reveal that the $\text{Ti}_3\text{C}_2\text{T}_x$ nanosheets are few-layered and very thin with the interlayer distance of approximately 1.35 nm (Fig. 1b-d). In addition, the BC suspension also shows stable colloid characteristics in very fine dispersion with apparent Tyndall effect (Figure S1). Figure 2a schematically depicts the fabrication process of sandwich-like TB film. Firstly, the $\text{Ti}_3\text{C}_2\text{T}_x$ and BC suspension were mixed with different mass ratios and vacuum filtered to form a hybrid film. Then, the sandwich-like TB film was obtained after cryogenic assembling and freeze-drying. The TB films with the mass ratios of $\text{Ti}_3\text{C}_2\text{T}_x$ and BC of 0.25, 0.5, 1.0, 1.5, 2.0 and 4.0 were denoted as TB-0.25, TB-0.5, TB-1, TB-1.5,

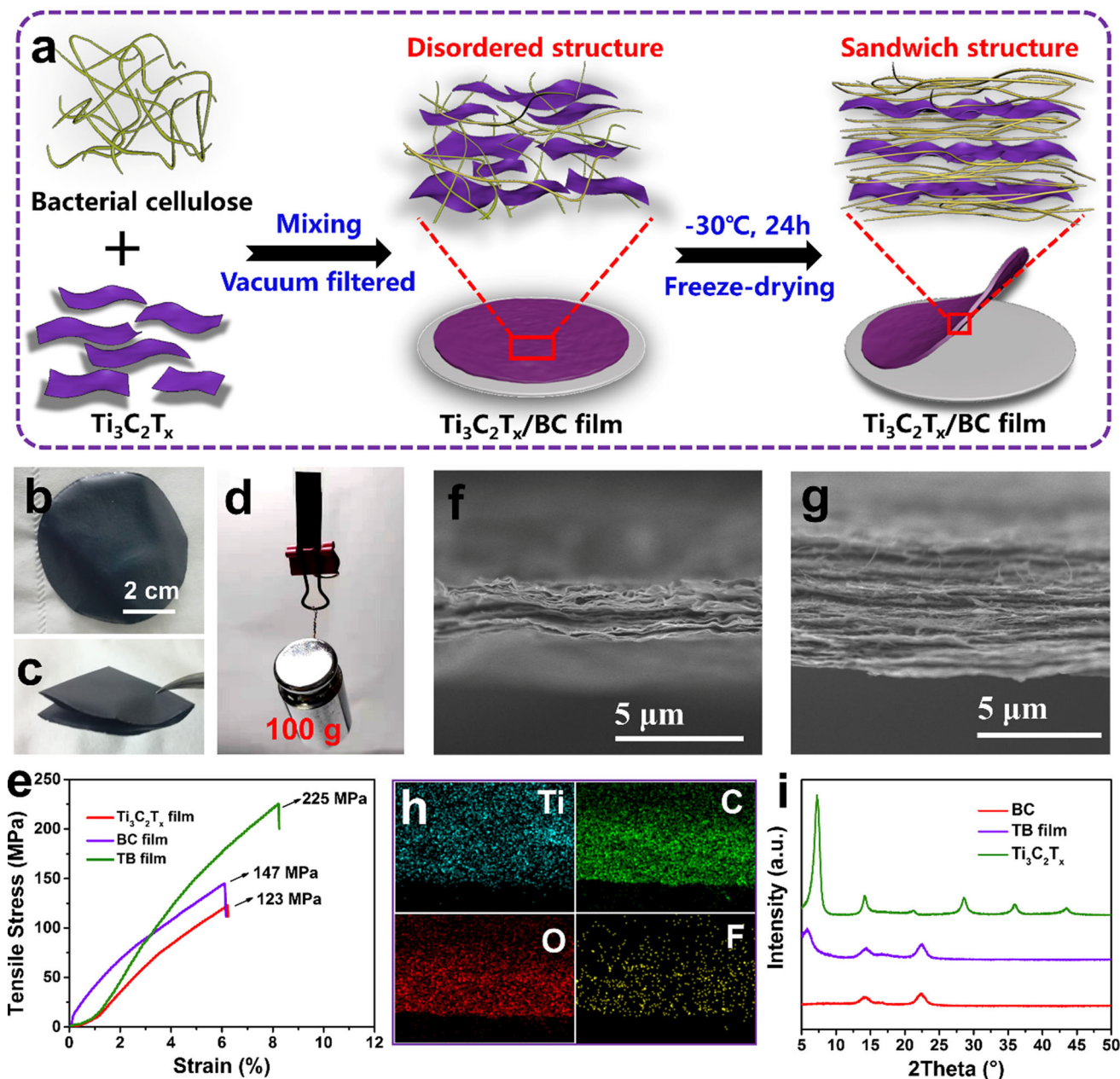


Figure 2 a Schematic representation of the fabrication of the TB film; the photographs of the as-prepared TB-0.25 film at **b** flat and **c** folded state; **d** A $3 \times 0.5 \text{ cm}^2$ TB-0.25 film hung a counterweight of 100 g; **e** tensile stress–strain curves of the pure

$\text{Ti}_3\text{C}_2\text{T}_x$, pure BC and TB-0.25 film; the cross-section SEM images of the **f** pure $\text{Ti}_3\text{C}_2\text{T}_x$ film; **g** TB-0.25 film and **h** the corresponding element distribution; **i** XRD patterns of pure BC, $\text{Ti}_3\text{C}_2\text{T}_x$ and TB-0.25 film.

TB-2 and TB-4, respectively. For comparison, individual $\text{Ti}_3\text{C}_2\text{T}_x$ and BC film were also prepared with same method. As found in our experimental process, the $\text{Ti}_3\text{C}_2\text{T}_x$ nanosheets can spontaneously absorb together with BC polymer chains owing to the strong hydrogen bond interactions of oxygen-containing functional groups on their surface, which is beneficial

to enhance the skeleton strength of sandwich-like hybrid film (Figure S2).

Figure 2b and c show the photographs of the TB-0.25 film at flat and folded states, demonstrating excellent flexibility. More interestingly, the prepared TB-0.25 film with a size of $3 \times 0.5 \text{ cm}^2$ can hang up a counterweight of 100 g (approximately 20,000 folds of its own weight) without obvious deformation or

cracking, showing good mechanical strength and strain adaptability as displayed in Fig. 2d. The stress–strain curves of pure $\text{Ti}_3\text{C}_2\text{T}_x$ film and TB film are quantitatively compared to better know their mechanical strength as shown in Fig. 2e and Table S1. The TB-0.25 film shows a maximum stress of ~ 225 MPa, which is superior to that of pure BC film (~ 147 MPa) and pure $\text{Ti}_3\text{C}_2\text{T}_x$ film (~ 123 MPa). The morphologies and microstructures of the TB-0.25 film and pure $\text{Ti}_3\text{C}_2\text{T}_x$ film were investigated by SEM. The cross-section SEM images of pure $\text{Ti}_3\text{C}_2\text{T}_x$ film and TB-0.25 film show a distinct difference as shown in Fig. 2f, g. It can be observed that the TB film presents a multilayered sandwich-like structure with many nanofibers wrapped by the nanosheets after cryogenic assembly compared to compact stacking structure of pure $\text{Ti}_3\text{C}_2\text{T}_x$ film. The hair-like BC nanofibers serve as a buffer layer to make the $\text{Ti}_3\text{C}_2\text{T}_x$ nanosheets-based hybrid film assembled tightly by hydrogen bond interactions and work like “flexible steel-reinforced concrete,” which greatly enhance the mechanical strength and flexibility. Meanwhile, the BC nanofibers intercalated into the MXene interlayer can bring in more interlayer space and improve the MXene utilization in the hybrid film. Element distribution mappings of C, O, F and Ti in the energy-dispersive spectrum (EDS) further indicate uniform distribution of $\text{Ti}_3\text{C}_2\text{T}_x$ nanosheets in the TB film (Fig. 2h). The phase characteristics were examined by X-ray diffraction (XRD) as shown in Fig. 2i. Two peaks located at 14.5° and $22.5^\circ(2\theta)$ are emerged in pure BC film and a strong peak located at 7.2° can be observed in pure $\text{Ti}_3\text{C}_2\text{T}_x$ film, corresponding to the microcrystal of cellulose and the (002) peak of $\text{Ti}_3\text{C}_2\text{T}_x$ nanosheets, respectively. In the TB-0.25 film, the (002) peak of $\text{Ti}_3\text{C}_2\text{T}_x$ film moves to a lower 2θ angle of 5.7° , attributing to the intercalation of BC into the $\text{Ti}_3\text{C}_2\text{T}_x$ interlayers and leading to the expansion of interlayer [21, 44].

Sensing performance characterization

In order to evaluate the pressure sensing performance, the prepared TB films with different contents of BC were cut into a piece of $5 \times 10 \text{ mm}^2$ attached on a flexible Au interdigital electrode and connected with an electrical sensing analyzer to record the real-time current signs. As mentioned above, the pressure sensitivity of TB-0.25, TB-0.5, TB-1.0, TB-1.5, TB-2.0 and TB-4.0 was investigated compared with that of

the pure MXene. It should be noted that the pure BC film could not be worked as pressure sensor because of its electrical insulation. Figure 3a and S3–8 demonstrate the sensitivity curves of different TB pressure sensors in the pressure range between 2 and 10,000 Pa. The sensitivity profiles of the TB pressure sensors show three regions with different slopes, which depend on the compressibility in different pressure ranges. In the low pressure ranges of less than 50 Pa, a small pressure loading can significantly change interlayer space and the resistance due to the relatively loose conductive networks, so high sensitivity can be obtained. With increasing the pressure, it becomes difficult to further greatly compress the conductive networks, resulting in the insignificant change of electrical resistance, so the sensitivity is reduced. Interestingly, the sensitivities in different pressure ranges are gradually increased with the increment of BC content (Fig. 3b). Compared to pure MXene, the TB-0.25 pressure sensor shows the highest values, indicating that the synergistic combination of BC greatly improves the pressure sensing performance of TB film. Specifically, a high sensitivity of 95.2 kPa^{-1} (denoted as S_1) is achieved in the pressure loading range of 2 to 50 Pa, which exceeds those of most of reported flexible carbon-based pressure sensor (See Table S2 for details) [7, 11, 12, 17, 19, 20, 43, 45–48]. When the pressure loading ranges from 50 to 3,000 Pa, the sensitivity of TB-0.25 pressure sensor (denoted as S_2) is about 27.5 kPa^{-1} . Even ranged in the pressure of higher than 3,000 Pa, the pressure sensor still can keep a sensitivity of 0.94 kPa^{-1} (denoted as S_3), indicating outstanding high sensitivity in the wide-sensing range. It is worth noting that the TB pressure sensor can also accurately distinguish tiny pressure loading. As illustrated in Figure S9, when the rice is loaded on TB sensor, the real-time current change displays a monotonic increase with increasing the rice grains, indicating the ultralow detection limit of 0.4 Pa. As shown in Table S2, the detection limit of the TB pressure sensor is quite low compared to those of most of the reported pressure sensors. Unless otherwise indicated, the TB-0.25 pressure sensor was selected for the other sensing performance evaluations. As shown in Fig. 3c and S10, the relative current change of the TB-0.25 pressure sensor distinctly increases with continuously increasing pressure loading in the range of $2 \sim 50$ Pa and $100 \sim 5000$ Pa, showing good response to different levels of

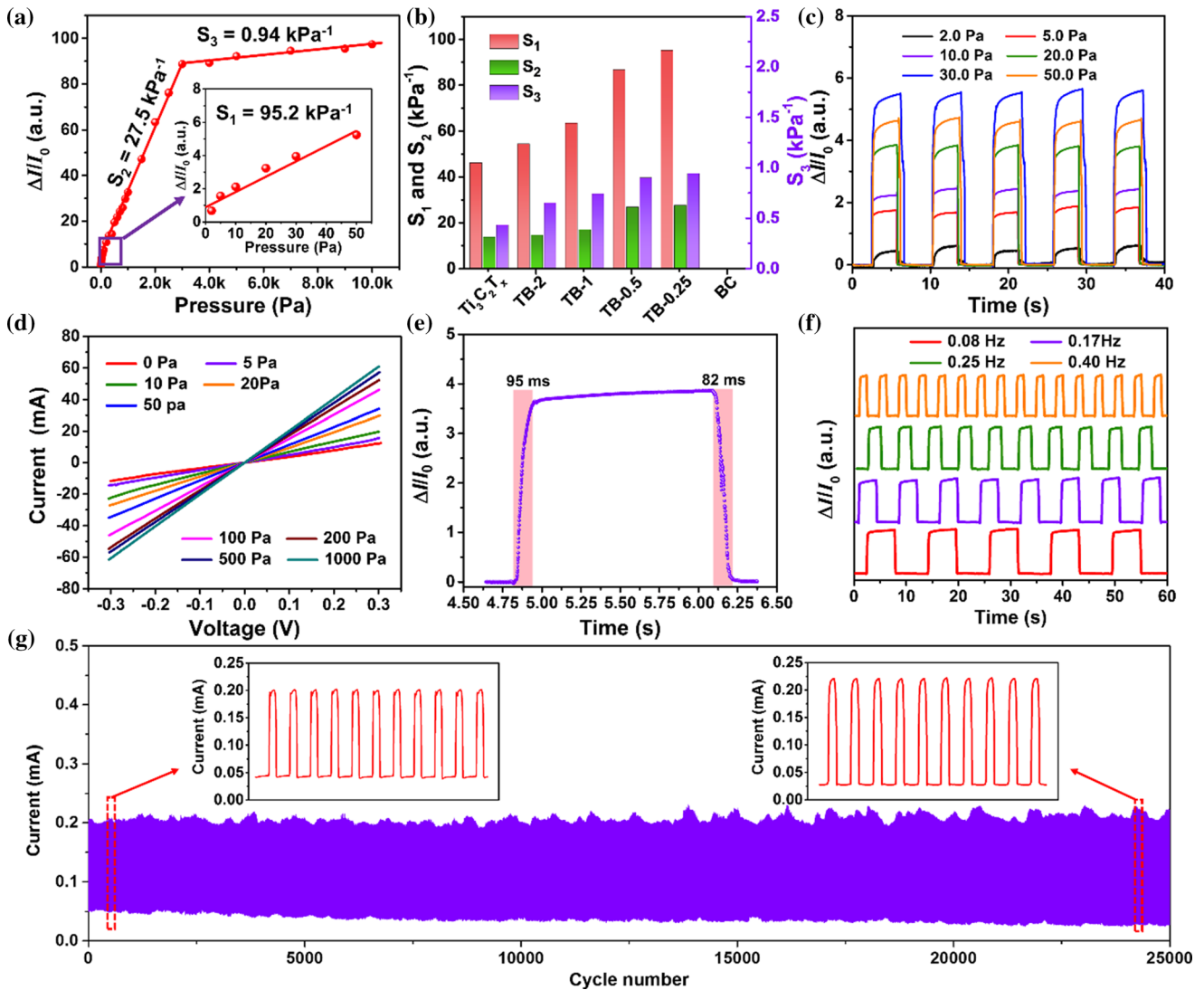


Figure 3 Sensing performance characterizations of TB pressure sensors. **a** Sensitivity of TB-0.25 pressure sensor in the pressure range of 2 to 10,000 Pa, the inset is the magnification of sensitivity curve in the range of 2~50 Pa; **b** sensitivity comparisons of TB samples with different BC contents in the range of 2~10,000 Pa; **c** relative current variation with increasing pressure from 2 to 50 Pa; **d** *I*-*V* curves of TB-0.25 pressure sensor under different

pressures; **e** response time and recovery time of TB pressure sensor under a pressure loading of 20 Pa; **f** real-time *I*-*t* curves of TB pressure sensor at different compression frequencies; **g** cyclic stability of TB pressure sensor for 25,000 loading-releasing cycles with a pressure loading of 200 Pa, the insets are the curves in the first and last ten cycles.

pressures and well agreeing with the results in Fig. 3a. Tested in a potential range of -0.3 to 0.3 V, the *I*-*V* curves show good linear relationship at different pressure loadings from 0 to 1000 Pa in Fig. 3d, revealing the relatively stable resistance and sensing performance at specific pressure loading. To understand the sensitivity of different thicknesses, we also prepared the TB-0.25 film with different thicknesses by adjusting the volume of Ti₃C₂T_x/BC dispersion. The sensitivity of the TB-0.25 films with thicknesses

of 4, 7 and 10 μm is exhibited in Figure S11. It can be seen that the current change under different pressure loadings has no significant difference and the sensitivities are independent on the thickness. Figure 3e shows the typical *I*-*t* curve of TB pressure sensor in the compression process of 20 Pa with a fast response time of ~95 ms and recovery time of ~82 ms without obvious hysteresis. Meanwhile, when the loading-releasing frequencies of the pressure increase from 0.08 to 0.4 Hz, the real-time *I*-*t* curves of TB

pressure sensors remain steady without obvious difference, revealing the fast response and instant recovery to high frequency pressure loading (Fig. 3f). Furthermore, the cyclic stability test of TB pressure sensor is evaluated by applying an interval pressure of 200 Pa. As shown in Fig. 3g, the current response signal maintains nearly identical amplitude with a little bit attenuation after 25000 cycles, demonstrating high stability and long-term operation adaptability. It is worth noting that this pressure sensor can normally operate at a low working voltage of 0.1 V, which endows the possibility to drive it by minitype wearable and portable energy accessories, demonstrating the potential application in self-powered integrated wearable electronics.

Furthermore, the sensing properties of the TB pressure sensor in the periodic bending–unbending process were also systematically investigated as shown in Fig. 4. Figure 4a shows the relative real-time current change of the TB pressure sensor in repetitive bending–unbending process with a bending angle of 45°. It is clearly observed that TB pressure sensor can have a quick current response and recovery to initial

state without distinct degradation in the continuously bending test, suggesting quick and stable response–recovery performance. Moreover, a series of real-time current–time changes with increasing bending angle from 5 to 60° are recorded (Fig. 4b). The current responses are obviously enhanced with increasing the bending angle, which is similar to the results in above pressure response, demonstrating good curling response performance. In addition, the sensor has a fast response time of ~ 119 ms to mechanical stimuli (Fig. 4c). I - V curves of TB pressure sensor at different bending angles from 5° to 120° show typical linear relationship in the potential windows of -0.3 to 0.3 V (Fig. 3d), indicating the stable sensing response under static bending stress. The slope of I - V curve keeps increasing with increment of bending angle, showing the corresponding increase in the conductivity. Even tested in different bending–unbending frequencies at a bending angle of 45°, the TB pressure sensor still can maintain a stable current response in the frequency increased from 0.08 to 0.4 Hz (Fig. 4e), indicating wide adaptability to bending stress in different frequencies. Figure 4f exhibits the cyclic test

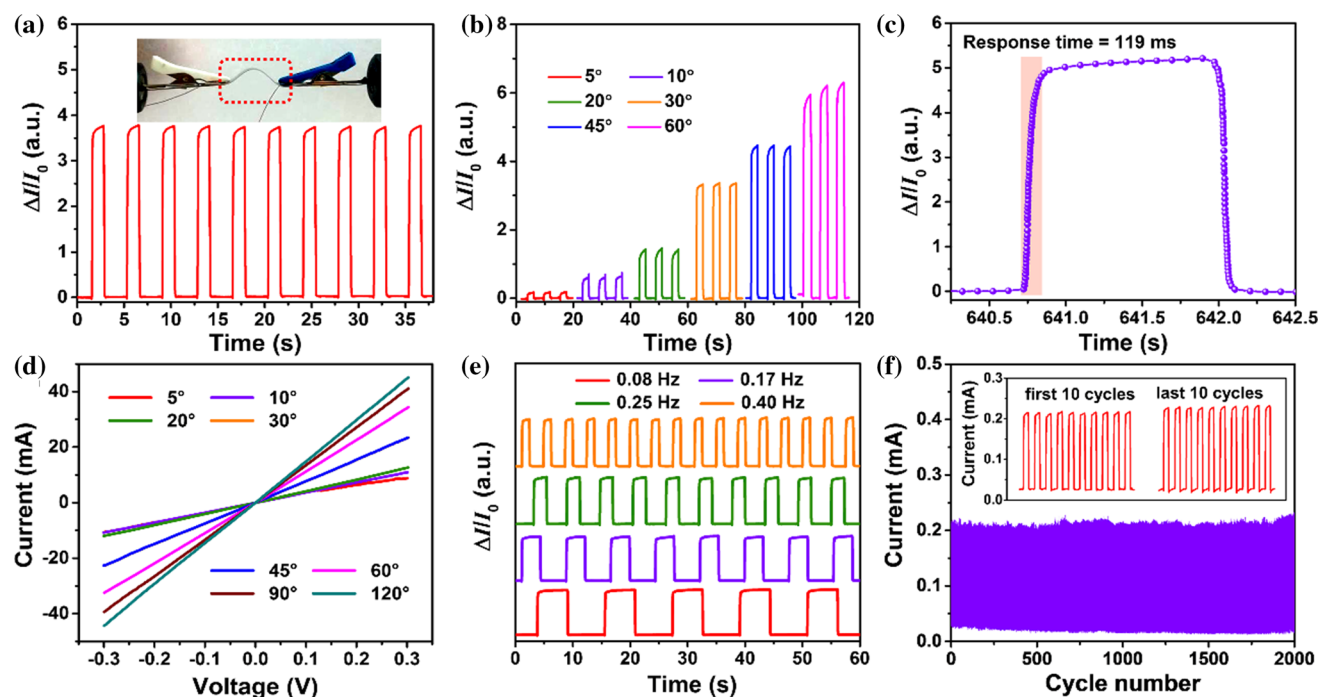


Figure 4 Sensing performance characterization of TB pressure sensor at different bending states. **a** Real-time I - t curves of TB pressure sensor in repetitive bending–unbending process, the inset is the photograph of TB pressure sensor at a bending angle of 45°; **b** the current–time curves with increasing bending angle from 5° to 60°; **c** response time of TB pressure sensor at a bending state; **d** I -

V curves of TB pressure sensor at different bending angles from 5° to 120°; **e** real-time I - t curves of TB pressure sensor in different bending–unbending frequencies at a bending angle of 45°; **f** repeatability of TB pressure sensor for 2,000 bending–unbending cycles at a frequency of 0.17 Hz with a bending angle of 45°, the insets are I - t curves of the first and last ten cycles.

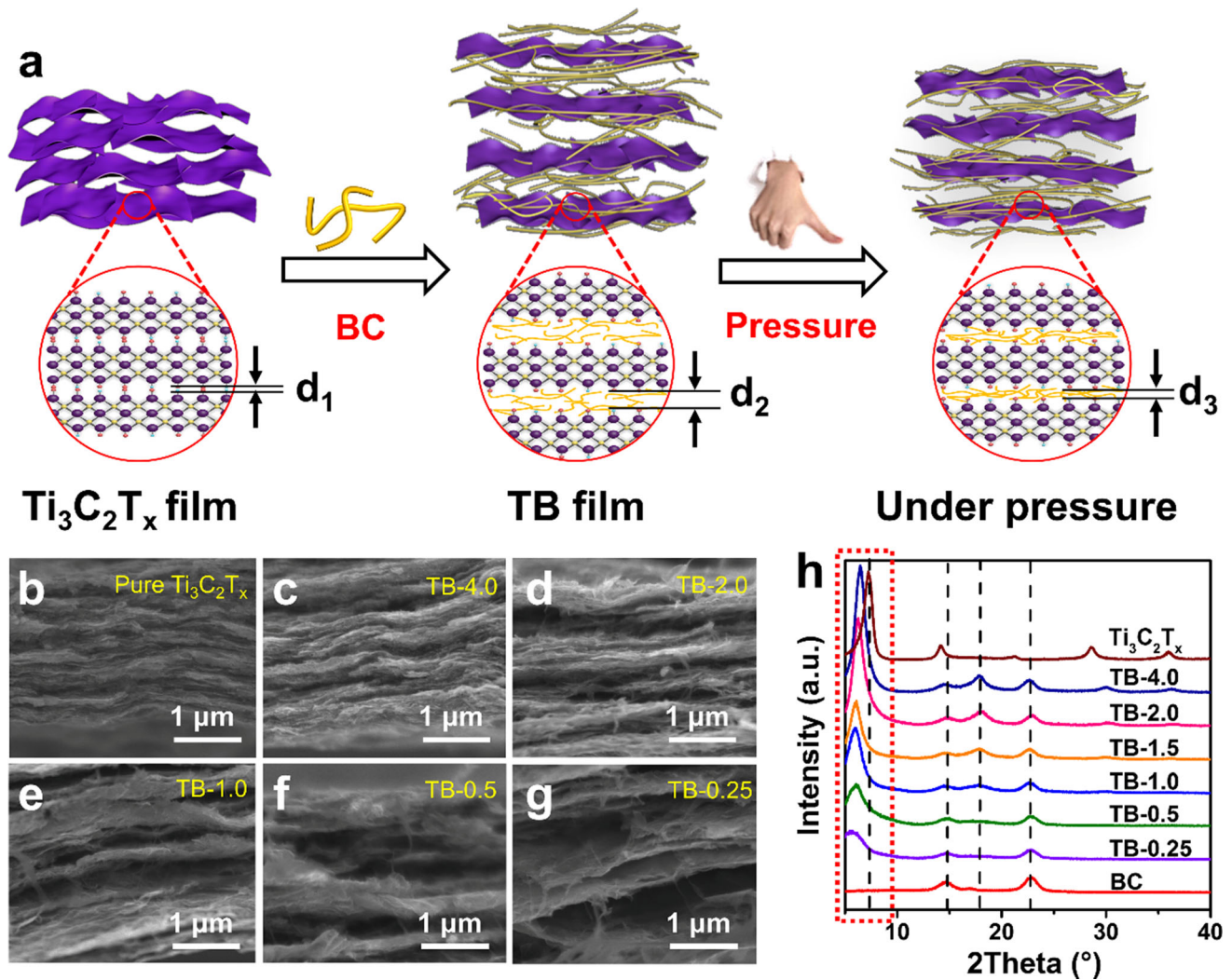


Figure 5 a Schematic illustration of the sensing mechanism of TB film pressure sensor; the cross-section images of **b** pure $\text{Ti}_3\text{C}_2\text{T}_x$, **c** TB-4.0, **d** TB-2.0, **e** TB-1.0 **f** TB-0.5 and **g** TB-0.25 film,

respectively; **h** XRD patterns of TB film with different MXene/BC mass ratios in the 2theta range of 5° to 40° .

of TB pressure sensor in the periodic bending–unbending process at a frequency of 0.17 Hz with a bending angle of 45° . As expected, the pressure sensor shows an excellent reproducibility as well as high signal-to-noise ratios for more than 2,000 cycles in the continuous bending–unbending test. Meanwhile, the current response outputs of the pressure sensor show negligible changes, further confirming high stability.

Analysis of the performance and structures

From the above results, it can be concluded that the enhanced sensing performance of TB pressure sensor is originated from the intercalation of the BC nanofibers into the MXene interlayers. The possible

mechanism is illustrated in Fig. 5a. The individual $\text{Ti}_3\text{C}_2\text{T}_x$ film presents obvious compact sandwich structure, which results in the limited change of layer spacing and a low resistance variation and sensitivity. The intercalation of the BC into the adjacent $\text{Ti}_3\text{C}_2\text{T}_x$ nanosheets can effectively separate and form a relatively loose multilayered structure with sufficient contact sites, leading to high sensitivity and flexibility. When loading a subtle pressure, the contact in the TB film is increased significantly and the interlayer distance is narrowed with the reduced tunneling resistance, thus achieving an obvious change in real-time current variation signal. To confirm this process, the sensitivities of the TB pressure sensor with different ratios of $\text{Ti}_3\text{C}_2\text{T}_x$ and BC are compared as

shown in Figure S12. The TB-0.25 film-based pressure sensor shows the highest sensitivity. To be specific, with an applied pressure of 200 Pa, the TB-0.25 film exhibits 37-fold pristine current variation and has much larger current variation under the same pressure, which is distinctly higher than that of other counterparts. At the same time, the cross-section morphologies of $\text{Ti}_3\text{C}_2\text{T}_x$ film with different BC contents are compared as shown in Fig. 5b–e. It is obvious that the distance between different $\text{Ti}_3\text{C}_2\text{T}_x$ nanosheets increases with the increment of BC content. In addition, the interlayer space variations of the prepared TB films with different BC contents are systematically examined by XRD (Fig. 5h). It can be seen that the peak centered at 7.2° attributable to (002) plane of pristine $\text{Ti}_3\text{C}_2\text{T}_x$ is successively changed to 6.5, 6.3, 6.2, 6.0, 5.9 and 5.7° for TB-4.0, TB-2.0, TB-1.5, TB-1.0, TB-0.5 and TB-0.25 film with the continuous increasing of the BC content, respectively, implying a continuous expanding of the interlayer spacing by the increase in BC content (Fig. 5f–g). These results demonstrate that the combination of BC nanofibers into the interlayer of few-layered $\text{Ti}_3\text{C}_2\text{T}_x$ results in the change of their interlayer distance and tunneling electrical resistance, thereby facilitating high sensing performance of the TB film.

Human motion detection

The outstanding sensing performance of the TB pressure sensor, especially in the low range pressure regions, makes it worked as a promising wearable sensor device for wide-range efficient human motion recognition. To demonstrate the potential application of TB sensor, the TB pressure sensor is attached to different positions of human body to record the real-time current signals as shown in Fig. 6. It is notable that the polyimide tape covered the upper surfaces to isolate and protect the TB sensor to direct contact with human skins. Figure 6a and c exhibit the real-time I - t curves of the TB pressure sensor measured in the different positions of body movements including finger, arm and knee bending, respectively. It could be seen that prompt and stable current responses with negligible current changes can be obtained during the periodic bending–stretching processes of finger, arm and knee, respectively. Additionally, thanks to the outstanding sensing performance in low range pressure region, subtle human biomedical signals including subtle pressures, e.g.,

swallow, heartbeat and pulse can also be clearly distinguished by the TB pressure sensor. As shown in Fig. 6d, e, the TB sensor attached to throat and chest position shows sensitive and repeatable current response with good stability. It is well known that the wrist pulse waveform is one of the crucial physiological parameters for monitoring the cardiovascular health condition. More interestingly, three distinct current peaks can be observed in the wrist pulse test (Fig. 6f and S13), corresponding to the percussion wave (P), tidal wave (T) and diastolic wave (D), respectively. The calculated beat frequency from the obtained pulse curves is about 73 bpm, which is in the normal beat range of the adult under static condition. These results further reveal that the TB pressures sensor can be potentially used in the diagnosis of the cardiovascular health and specific disease. At the same time, the TB pressure sensor shows sensitive response to the acoustic vibration signals. As shown in Fig. 6g, the TB pressure sensor is fixed in the larynx position. Different sounds can produce the corresponding vibrations of the sensor, so the sounds can be detected and distinguished from the recorded current signals. Some words such as “MXene” and “Sensor” can be detected and distinguished accurately and the current response for the same word shows quite similar peak characteristics in the repetitive three cycles, further demonstrating high sensitivity and repeatability in the acoustic recognition. Furthermore, while the finger is continuously bent to different deformation states, the recorded signal shows distinct response current with increased values accompanying with the increased bending angles (Fig. 6h). These results demonstrate that the TB pressure sensor can be potentially used in wearable sensor electronics to monitor the pressure, bending and acoustic forces with high sensitivity, good stability and wide adaptability.

Furthermore, combining multiple TB pressure sensors into special assembly can be applied to detect the tactile signals and map spatial pressure distribution for electronic skin. As exhibited in Fig. 7a, b, by integrating TB sensors on five fingertips of rubber glove, respectively, tactile signals of different gestures such as holding and grasping of objects can be collected, which is a prerequisite for building the artificial robotics. The TB sensor can precisely measure the response signals of every finger motion and recognize unique current response for different gestures including holding cylinder, spreading five

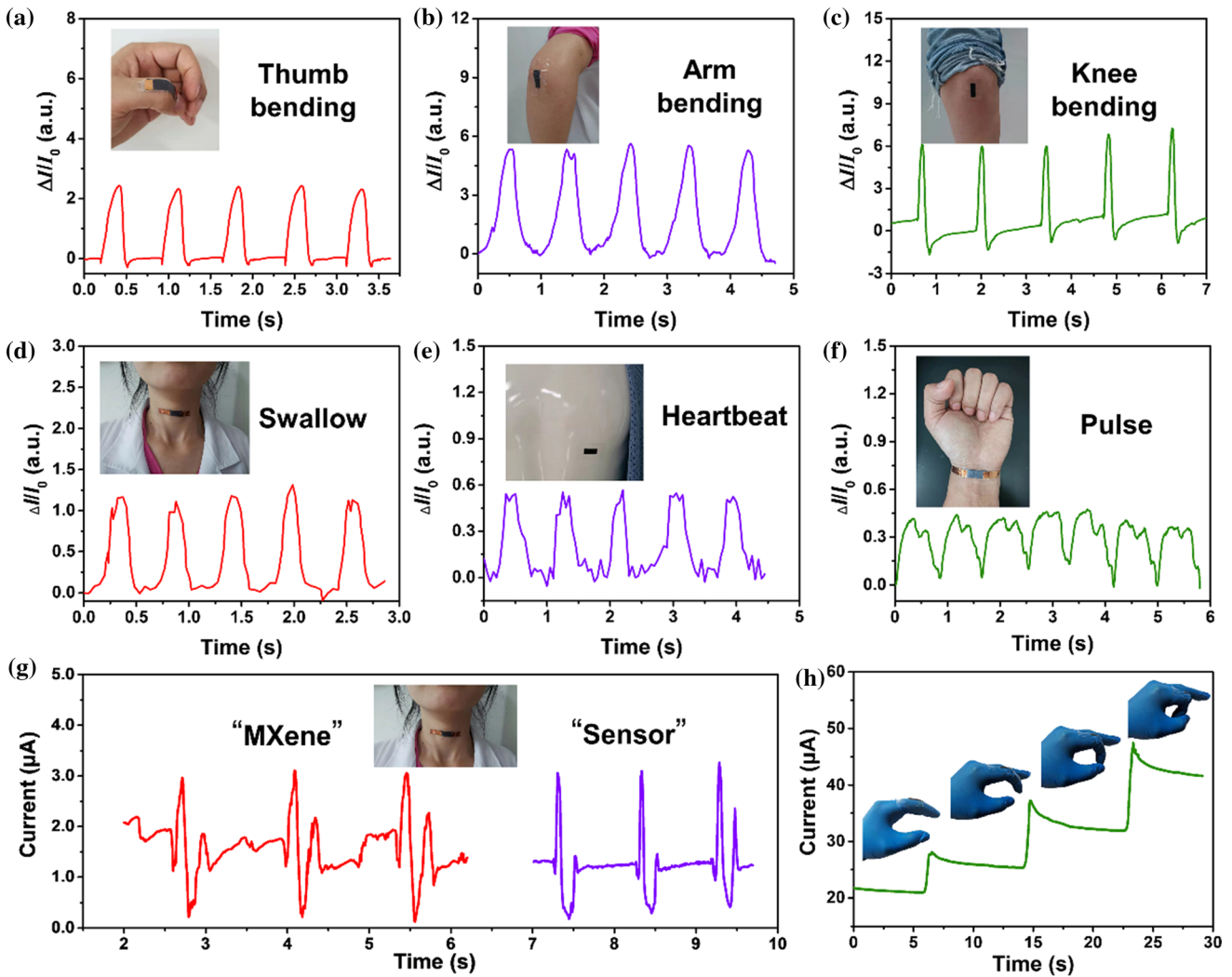


Figure 6 Flexible TB pressure sensor for monitoring various human motions including subtle pressures, e.g., swallow, heartbeat and pulse, acoustic vibrations and bending deformations etc. Real-time current-time curves of **a** finger, **b** arm and **c** knee bending, respectively; current-time curves of subtle human motions

including **d** swallowing, **e** heartbeat and **f** pulse, respectively; **g** acoustic vibrations from speaking different words (“MXene” and “sensor”), respectively; **h** real-time current-time curves in the process of continuous bent finger with the increased bending angles.

fingers, pinching clamp and holding mouse (Fig. 7b). In addition, a flexible 3×3 TB film-based pixel array is fabricated to detect the mapping pressure distribution by pasting the TB film on interdigital electrodes based on polyimide (PI) substrate, which can be greatly bent (Fig 7c, d). It is noteworthy that each pixel cannot interfere with each other in the whole system and the real-time current change exhibits little difference for individual sensor (Figure S14). When the object contacts with the sensor array surface, the touch points of the objects are recognized by recording the real-time current signal of each pixel. As shown in Fig. 7e-h, the pixel sensor array can

accurately monitor and recognize the pressure distribution of different objects. Specifically, when placed a screw and a plastic cap on the 3×3 pixel sensor arrays, the corresponding output current signal of each pixel was measured and recorded. As shown in Fig. 7f, h, the mapping spatial pressure distribution is well presented with a clear color contrast, which agrees with the actual object position. The high resolution of mapping spatial pressure distribution makes the TB pressure sensor promising application in multifunctional sensor electronics and human-machine interfacing.

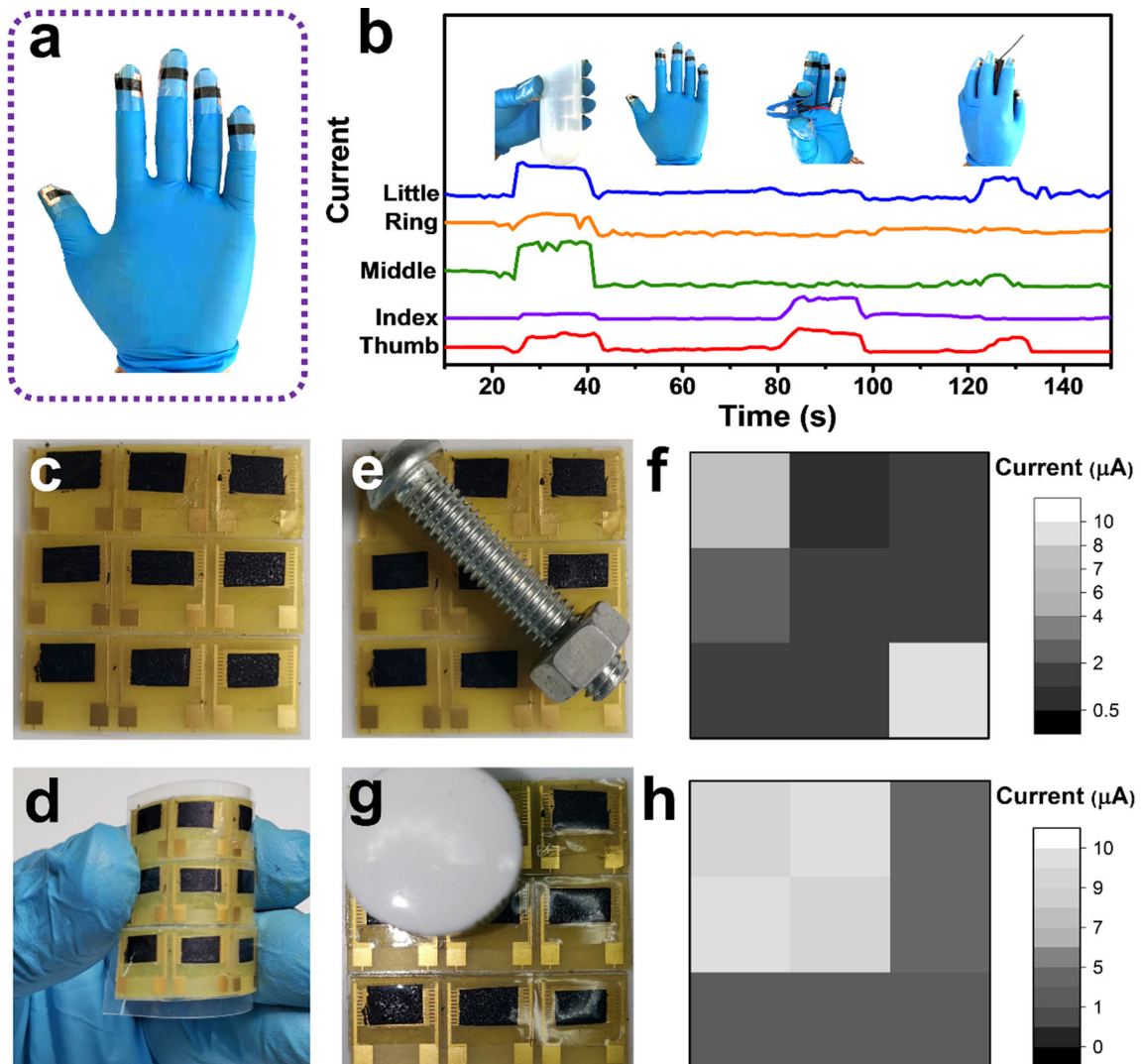


Figure 7 **a** Photograph of integrating five skin sensors attached on the fingertips of rubber glove; **b** real-time current-time curves of the pressure sensors on different fingertips at different motions states; photographs of 3×3 pressure sensor array at **c** flat and

d bent states, respectively; **e** a screw and **g** a plastic cap placed on the 3×3 pressure sensor array and **f**, **h** corresponding map distribution, respectively. The color contrast mappings agree with the object position.

Conclusion

In summary, we successfully developed a MXene-BC hybrid film-based pressure sensor with high mechanical strength and excellent sensing performance by a simple and efficient nanocellulose intercalated strategy. The combination of BC nanofibers serves as a highly flexible buffer to promote the layer separation of MXene and bring in more interlayer spaces and efficient MXene utilization, thus significantly enhancing the sensing activities. The prepared TB pressure sensor presents a high sensitivity (up to 95.2 kPa^{-1} in $<50 \text{ Pa}$), fast response (95 ms), wide-

sensing range with a low-detection limit ($0.4 \sim 10,000 \text{ Pa}$) and a low operation voltage (0.1 V) as well as good repeatability without obvious degradation up to 25000 cycles. These outstanding sensing performances are capable of detecting both normal pressures, bending force and various subtle pressures in different human physiological activities including the heartbeat, pulse, swallow and acoustic vibrations. More importantly, the TB pressure sensor can also discriminate and map the spatial pressure distribution with high resolution and sensitivity. These results indicate that the pressure sensor is a

promising candidate for application in health-care electronics, E-skin and human-machine interfacing.

Acknowledgements

The authors acknowledge the financial supports by NSAF (Grant No. U1930205), National Natural Science Foundation of China (Nos. 21875226, 52072352, U20A2072), the Foundation for the Youth S&T Innovation Team of Sichuan Province (2020JDTD0035), Tianfu Rencai Plan, the Chengdu Talent plan, Science and Technology Projects for Administration for Market Regulation of Sichuan Province (SCSJ2020016) and the Talent Plan of China Science City.

Author contributions

J. Yang, J.L. Cheng and B. Wang designed the research; J. Yang conducted the experiments; J. Yang, J.L. Cheng and B. Wang analyzed the data and wrote the manuscript; H. Li, J.S. Li and T. He discussed and edited the manuscript; All the authors discussed the results and commented on this paper.

Data availability

All data associated with the study are included in main text and supplementary information. Additional information is available from the correspondence upon reasonable request.

Compliance with ethical standard

Conflict of interest The authors declare no competing financial interest

Supplementary Information: The online version contains supplementary material available at <http://doi.org/10.1007/s10853-021-05909-y>.

References

- [1] Bu T, Xiao T, Yang Z, Liu G, Fu X, Nie J, Guo T, Pang Y, Zhao J, Xi F (2018) Stretchable Triboelectric-photonic smart skin for tactile and gesture sensing. *Adv Mater* 30:e1800066. <https://doi.org/10.1002/adma.201800066>
- [2] Tai LC, Gao W, Chao M, Bariya M, Ngo QP, Shahpar Z, Nyein H, Park YY, Sun HJ, Jung Y (2018) Methylxanthine drug monitoring with wearable sweat sensors. *Adv Mater* 30:e1707442. <https://doi.org/10.1002/adma.201707442>
- [3] Carvalho AF, Fernandes AJS, Leitão C, Deuermeier J, Marques AC, Martins R, Fortunato E, Costa FM (2018) Laser-induced graphene strain sensors produced by ultraviolet irradiation of polyimide. *Adv Funct Mater* 28:1805271. <https://doi.org/10.1002/adfm.201805271>
- [4] Wang Z, Guan X, Huang H, Wang H, Lin W, Peng Z (2019) Full 3D printing of stretchable piezoresistive sensor with hierarchical porosity and multimodulus architecture. *Adv Funct Mater* 29:1807569. <https://doi.org/10.1002/adfm.201807569>
- [5] Tai Y, Lubineau G (2017) Human-finger electronics based on opposing Humidity-resistance responses in carbon nanofilms. *Small* 13:1603486. <https://doi.org/10.1002/sml.201603486>
- [6] Li S, Pan N, Zhu Z, Li R, Li B, Chu J, Li G, Chang Y, Pan T (2019) All-in-One iontronic sensing paper. *Adv Funct Mater* 29:1807343. <https://doi.org/10.1002/adfm.201807343>
- [7] Guo Y, Zhong M, Fang Z, Wan P, Yu G (2019) Wearable transient pressure sensor made with MXene nanosheets for sensitive Broad-range Human-machine interfacing. *Nano Lett* 19:1143–1150. <https://doi.org/10.1021/acs.nanolett.8b04514>
- [8] Qiu A, Li P, Yang Z, Yao Y, Le I, Ma J (2019) A Path beyond metal and silicon: Polymer/Nanomaterial composites for stretchable strain sensors. *Adv Funct Mater* 29:1806306. <https://doi.org/10.1002/adfm.201806306>
- [9] Wang T, Zhang Y, Liu Q, Cheng W, Wang X, Pan L, Xu B, Xu H (2018) A Self-healable, highly stretchable, and solution processable conductive polymer composite for ultra-sensitive strain and pressure sensing. *Adv Funct Mater* 28:1705551. <https://doi.org/10.1002/adfm.201705551>
- [10] Ha M, Lim S, Ko H (2018) Wearable and flexible sensors for user-interactive health-monitoring devices. *J Mater Chem B* 6:4043–4064. <https://doi.org/10.1039/C8TB01063C>
- [11] Pang Y, Zhang K, Yang Z, Jiang S, Ju Z, Li Y, Wang X, Wang D, Jian M, Zhang YY, Ren TL (2018) Epidermis microstructure inspired graphene pressure sensor with random distributed spinosum for high sensitivity and large linearity. *ACS Nano* 12:2346–2354. <https://doi.org/10.1021/acsnano.7b07613>
- [12] Tao LQ, Zhang KN, Tian H, Liu Y, Wang DY, Chen Y, Yang QY, Ren TL (2017) Graphene-paper Pressure sensor for detecting human motions. *ACS Nano* 11:8790–8795. <http://doi.org/10.1021/acsnano.7b02826>

- [13] D'Elia E, Barg S, Ni N, Rocha VG, Saiz E (2015) Self-healing graphene-based composites with sensing capabilities. *Adv Mater* 27:4788–4794. <https://doi.org/10.1002/adma.201501653>
- [14] Yan T, Wang Z, Pan ZJ (2018) Flexible strain sensors fabricated using carbon-based nanomaterials: A review. *Curr Opin Solid State Mater Sci* 22:213–228. <https://doi.org/10.1016/j.cossms.2018.11.001>
- [15] Gao L, Zhu C, Li L, Zhang C, Liu J, Yu HD, Huang W (2019) All Paper-based flexible and wearable piezoresistive pressure sensor. *ACS Appl Mater Interfac* 11:25034–25042. <https://doi.org/10.1021/acsami.9b07465>
- [16] Yao S, Ren P, Song R, Liu Y, Huang Q, Dong J, O'Connor BT, Zhu Y (2020) Nanomaterial-enabled flexible and stretchable sensing systems: processing, integration, and applications. *Adv Mater* 32:1902343. <https://doi.org/10.1002/adma.201902343>
- [17] Wang Q, Jian M, Wang C, Zhang YY (2017) Carbonized silk nanofiber membrane for transparent and sensitive electronic skin. *Adv Funct Mater* 27:1605657. <https://doi.org/10.1002/adfm.201605657>
- [18] Lv L, Zhang P, Xu T, Qu L (2017) Ultrasensitive pressure sensor based on an ultralight sparkling graphene block. *ACS Appl Mater Interfac* 9:22885–22892. <https://doi.org/10.1021/acsami.7b07153>
- [19] Chen S, Song Y, Xu F (2018) Flexible and highly sensitive resistive pressure sensor based on carbonized crepe paper with corrugated structure. *ACS Appl Mater Interfac* 10:34646–34654. <https://doi.org/10.1021/acsami.8b13535>
- [20] Ma Y, Liu N, Li L, Hu X, Zou Z, Wang J, Luo S, Gao Y (2017) A highly flexible and sensitive piezoresistive sensor based on MXene with greatly changed interlayer distances. *Nat Commun* 8:1207. <https://doi.org/10.1038/s41467-017-01136-9>
- [21] Wang Y, Wang X, Li X, Bai Y, Xiao H, Liu Y, Liu R, Yuan G (2019) Engineering 3D Ion transport channels for flexible MXene films with superior capacitive performance. *Adv Funct Mater* 29:1900326. <https://doi.org/10.1002/adfm.201900326>
- [22] Wang H, Li L, Zhu C, Lin S, Wen J, Jin Q, Zhang X (2018) In situ polymerized Ti_3C_2Tx/PDA electrode with superior areal capacitance for supercapacitors. *J Alloy Compd* 778:858–865. <https://doi.org/10.1016/j.jallcom.2018.11.172>
- [23] Huang H, He J, Wang ZX, Zhang HT, Jin L, Chen N, Xie Y, Chu X, Gu B, Deng W, Yang W (2020) Scalable, and low-cost treating-cutting-coating manufacture platform for MXene-based on-chip micro-supercapacitors. *Nano Energy* 69:104431. <https://doi.org/10.1016/j.nanoen.2019.104431>
- [24] Tang X, Guo X, Wu W, Wang G (2018) 2D Metal carbides and nitrides (MXenes) as High-performance electrode materials for Lithium-based batteries. *Adv Energy Mater* 8:1801897. <https://doi.org/10.1002/aenm.201801897>
- [25] Zhang X, Lv R, Wang A, Guo W, Liu X, Luo J (2018) MXene Aerogel scaffolds for High-rate lithium metal anodes. *Angew Chem Int Ed* 57:15028–15033. <https://doi.org/10.1002/anie.201808714>
- [26] Wang H, Wu Y, Yuan X, Zeng G, Zhou J, Wang X, Chew JW (2018) Clay-inspired MXene-based electrochemical devices and Photo-electrocatalyst: State-of-the-Art progresses and challenges. *Adv Mater* 30:1704561. <https://doi.org/10.1002/adma.201704561>
- [27] Li X, Wang C, Cao Y, Wang G (2018) Functional MXene materials: progress of their applications. *Chem Asian J* 13:2742–2757. <https://doi.org/10.1002/asia.201800543>
- [28] Gao YY, Yan C, Huang HC, Yang T, Tian G, Xiong D, Chen NJ, Chu X, Zhong S, Deng W, Fang Y, Yang WQ (2020) Microchannel-confined MXene based flexible piezoresistive multifunctional Micro-Force sensor. *Adv Funct Mater* 30:1909603. <https://doi.org/10.1002/adfm.201909603>
- [29] Wang K, Lou Z, Wang LL, Zhao LJ, Zhao SF, Wang DY, Han W, Jiang K, Shen GZ (2019) Bioinspired interlocked Structure-induced high deformability for Two-dimensional titanium carbide (MXene)/natural Microcapsule-based flexible pressure sensors. *ACS Nano* 13:9139–9147. <https://doi.org/10.1021/acs.nano.9b03454>
- [30] Zhang Y, Chang TH, Jing L, Li KR, Yang HT, Chen PY (2020) Heterogeneous, 3D Architecturing of 2D titanium carbide (MXene) for microdroplet manipulation and voice recognition. *ACS Appl Mater Interfac* 12:8392–8402. <https://doi.org/10.1021/acsami.9b18879>
- [31] Sharma S, Chhetry A, Sharifuzzaman M, Yoon H, Park JY (2020) Wearable capacitive pressure sensor based on MXene composite nanofibrous scaffolds for reliable human physiological signal acquisition. *ACS Appl Mater Interfac* 12:22212–22224. <https://doi.org/10.1021/acsami.0c05819>
- [32] Wang L, Zhang MY, Yang B, Tan JJ, Ding XY (2020) Highly compressible, thermally stable, Light-weight and robust aramid Nanofibers/ Ti_3AlC_2 MXene composite aerogel for sensitive pressure sensor. *ACS Nano* 14:10633–10647. <https://doi.org/10.1021/acs.nano.0c04888>
- [33] Zhu M, Yue Y, Cheng YF, Zhang YN, Su J, Long F, Jiang XL, Ma YN, Gao YH (2020) Hollow MXene Sphere/Reduced graphene aerogel composites for piezoresistive sensor with Ultra-high sensitivity. *Adv Electron Mater* 6:1901064. <https://doi.org/10.1002/aelm.201901064>
- [34] Yue Y, Liu NS, Liu WJ, Li M, Ma YN, Luo C, Wang SL, Rao JY, Hu XK, Su J, Zhang Z, Huang Q, Gao YH (2018) 3D hybrid porous MXene-sponge network and its application in piezoresistive sensor. *Nano Energy* 50:79–87. <https://doi.org/10.1016/j.nanoen.2018.05.020>

- [35] Ma Y, Yue N, Zhang Y, Cheng HF, Zhao WQ, Rao JY, Luo SJ, Wang J, Jiang XL, Liu ZT, Liu NS, Gao YH (2018) 3D Synergistical MXene/Reduced graphene oxide aerogel for a piezoresistive sensor. *ACS Nano* 12:3209–3216. <https://doi.org/10.1021/acsnano.7b06909>
- [36] Zhuo H, Hu YJ, Chen ZH, Peng XW, Liu LX, Luo QS, Yi JW, Liu CF, Zhong LX (2019) A carbon aerogel with super mechanical and sensing performances for wearable piezoresistive sensors. *J Mater Chem A* 7:8092–8100. <https://doi.org/10.1039/c9ta00596j>
- [37] Li L, Fu XY, Chen S, Uzun S, Levitt AS, Shuck CE, Han W, Gogotsi Y (2020) Hydrophobic and stable MXene-polymer pressure sensors for wearable electronics. *ACS Appl Mater Interfac* 12:15362–15369. <https://doi.org/10.1021/acsnano.0c00255>
- [38] Cai Y, Shen J, Ge G, Zhang Y, Jin W, Huang W, Shao J, Yang J, Dong X (2018) Stretchable $Ti_3C_2T_x$ MXene/Carbon nanotube composite based strain sensor with ultrahigh sensitivity and tunable sensing range. *ACS Nano* 12:56–62. <https://doi.org/10.1021/acsnano.7b06251>
- [39] Shi XL, Wang HK, Xie XT, Xue QW, Zhang JY, Kang SQ, Wang CH, Liang J, Chen YS (2019) Bioinspired ultrasensitive and stretchable MXene-based strain sensor via Nacre-mimetic microscale “Brick-and-Mortar” architecture. *ACS Nano* 13:649–659. <https://doi.org/10.1021/acsnano.8b07805>
- [40] Hosseini H, Kokabi M, Mousavi SM (2018) Conductive bacterial cellulose/multiwall carbon nanotubes nanocomposite aerogel as a potentially flexible lightweight strain sensor. *Carbohydr Polym* 201:228–235. <https://doi.org/10.1016/j.carbpol.2018.08.054>
- [41] Gao C, Wan Y, He F, Liang H, Luo H, Han J (2010) Mechanical, moisture absorption, and photodegradation behaviors of bacterial cellulose Nanofiber-reinforced unsaturated polyester composites. *Adv Polym Technol* 30:249–256. <https://doi.org/10.1002/adv.20220>
- [42] Andrade FK, Moreira SM, Domingues L, Gama FM (2010) Improving the affinity of fibroblasts for bacterial cellulose using carbohydrate-binding modules fused to RGD. *J Biomed Mater Res A* 92:9–17. <https://doi.org/10.1002/jb.m.a.32284>
- [43] Chen Z, Hu Y, Zhuo H, Liu L, Jing S, Zhong L, Peng X, Sun RC (2019) Compressible, elastic, and Pressure-sensitive carbon aerogels derived from 2D titanium carbide nanosheets and bacterial cellulose for wearable sensors. *Chem Mater* 31:3301–3312. <https://doi.org/10.1021/acs.chemmater.9b00259>
- [44] Ding L, Wei Y, Li L, Zhang T, Wang H, Xue J, Ding LX, Wang S, Caro J, Gogotsi Y (2018) MXene molecular sieving membranes for highly efficient gas separation. *Nat Commun* 9:155. <https://doi.org/10.1038/s41467-017-02529-6>
- [45] Sun QJ, Zhao XH, Zhou Y, Yeung CC, Wu W, Venkatesh S, Xu ZX, Wylie JJ, Li WJ, Roy VAL (2019) Fingertip-Skin-Inspired highly sensitive and multifunctional sensor with hierarchically structured conductive Graphite/Polydimethylsiloxane foams. *Adv Funct Mater* 29:1808829. <https://doi.org/10.1002/adfm.201808829>
- [46] Yang K, Yin F, Xia D, Peng H, Yang J, Yuan W (2019) A highly flexible and multifunctional strain sensor based on a network-structured MXene/polyurethane mat with ultra-high sensitivity and a broad sensing range. *Nanoscale* 11:9949–9957. <https://doi.org/10.1039/C9NR00488B>
- [47] Jian M, Xia K, Wang Q, Yin Z, Wang H, Wang C, Xie H, Zhang M, Zhang Y (2017) Flexible and highly sensitive pressure sensors based on bionic hierarchical structures. *Adv Funct Mater* 27:1606066. <https://doi.org/10.1002/adfm.201606066>
- [48] Shi J, Wang L, Dai Z, Zhao L, Du M, Li H, Fang Y (2018) Multiscale hierarchical design of a flexible piezoresistive pressure sensor with high sensitivity and wide linearity range. *Small* 14:1800819. <https://doi.org/10.1002/smll.201800819>

Publisher's Note Springer Nature remains neutral with regard to jurisdictional claims in published maps and institutional affiliations.